

The Influence of Al Content and Thickness on the Microstructure and Tensile Properties in High-Pressure Die Cast Magnesium Alloys



ERIN DEDA, TRACY D. BERMAN, and JOHN E. ALLISON

The influence of Al content and section thickness on the microstructural features and tensile properties of high-pressure die cast AM series magnesium alloys is quantified in order to better understand the relationship between microstructure and tensile properties. It is found that with increasing aluminum content, the yield strength increases and the ductility decreases. Increasing the plate thickness results in a decrease in both the yield strength and ductility. The grain size, β -Mg₁₇Al₁₂ phase volume fraction, and solute content are all quantified through the thickness of the plates. It is found that the plates have a skin with increased hardness, due to a fine grain structure. The primary factors affecting strengthening in these alloys, including microstructural variations through the thickness, are accounted for using a linear superposition model. We conclude that yield strength is dominated by grain boundary strengthening and solid solution strengthening effects. The through-thickness grain size and solute concentration were quantified and these variations were found to play an important role in controlling the yield strength of these alloys.

DOI: 10.1007/s11661-017-3958-4

© The Minerals, Metals & Materials Society and ASM International 2017

I. INTRODUCTION

DUE to their high specific strength and good castability, magnesium alloys are desirable for use in weight reduction strategies for automotive applications.^[1,2] Over 95 pct of magnesium parts for structural applications are manufactured using the high-pressure die casting process.^[3,4] High-pressure die casting (HPDC) allows large, thin-walled components to be mass-produced rapidly and economically. In HPDC, highly turbulent molten metal flows into the shaped die cavity, generating a broad distribution of microstructures through the thickness and in different regions of a single casting.^[5,6] The heterogeneity observed in the microstructure of cast components leads to increased variability in the observed tensile properties as shown by Forsmark *et al.*^[7]

The use of magnesium alloy die castings is limited partially by the variability in mechanical properties observed in HPDC components.^[8] This variability necessitates conservatively designed HPDC parts and limits the ability to use HPDC components in crash-sensitive applications where ductility and deformation behavior are especially important. It is commonly believed that these properties, particularly the ductility, strongly depend on porosity levels.^[9–11] For this reason, super vacuum die casting (SVDC) technology is being explored to minimize the presence of gas porosity and in

turn improve the mechanical properties.^[3] To take full advantage of the property improvements provided by SVDC, there is a need for improved predictability of properties.

In order to better predict location-dependent properties in castings, integrated computational materials engineering (ICME) approaches are under development.^[12] Currently, two approaches exist to capture and reduce variations in properties—“quality mapping” statistical approaches and deterministic physics-based structure–property relationships. Quality mapping is an empirical approach currently used to capture spatial property variation within a casting using highly calibrated parameters.^[13–15] Since the quality mapping approach is not physics-based, it can be difficult to extrapolate results beyond the range of model calibration. This approach also requires a large quantity of experimental data. Thus, further study of the fundamental effects of microstructure on the tensile properties is needed to develop physics-based models for use in more refined ICME tools. Recently, deterministic yield strength models have been developed by Yang *et al.*, Sharifi *et al.*, and Toda-Carabello *et al.*^[16–18] These models incorporate known strengthening mechanisms, specifically grain boundary, solid solution, and dispersion strengthening, but use different methods to calculate each strength component.^[19]

To better understand the mechanical properties, it is important to understand both intrinsic and extrinsic microstructural features throughout the entire casting.^[20] Intrinsic microstructural features are those that are related to the composition of the alloy, such as composition variation and formation of eutectic phases. Extrinsic features are those that are related to the

ERIN DEDA, TRACY D. BERMAN, and JOHN E. ALLISON are with the University of Michigan, Ann Arbor, MI 48109. Contact e-mail: ededa@umich.edu

Manuscript submitted October 3, 2016.

Article published online January 20, 2017

manufacturing process. These features are produced and controlled by the casting process, including shrinkage- and microporosity, inhomogeneous microstructures [e.g., externally solidified crystals (ESCs)], casting defects (e.g., oxide films, hot tearing), and the development of skin and core microstructures. Of particular importance is the occurrence of ESCs in the core, which are coarse, dendritic grains that solidify before entering the die cavity.

Tensile properties appear to be a function of a hierarchy of effects from the different microstructural features. For example, there is an observed dependence of the mechanical behavior on intrinsic features due to alloying effects as observed by Aune *et al.*^[21] The most deleterious features tend to be oxide films and large pores which result in a significant reduction of the ductility,^[22] while β -Mg₁₇Al₁₂ volume fraction and morphology are likely to only have a minor impact on mechanical properties.^[23] Characterizing critical microstructural features as inputs to current and future models for the tensile properties is an important step to refining prediction of the yield strength and in the future, ductility.

In this study, we quantify the influence of Al content and plate thickness on the microstructural features and tensile properties of a series of SVDC aluminum-manganese (AM-type) magnesium alloys. SVDC was used to reduce the influence of extrinsic microstructural feature such as entrapped gas porosity. These results are used to evaluate the efficacy of an improved analytical model for strength. The results from this investigation were designed as inputs to parallel investigations using crystal plasticity and continuum mechanics simulations of microstructural influences on the ductility.^[11,24,25]

II. EXPERIMENTAL

Mg-Al-Mn alloy (AM series magnesium alloys) plates were super-vacuum die cast by Ford Research and Innovation Center at MagTech Corporation. Plates of nominal dimensions 305 mm × 130 mm (12 inch × 5 inch) were cast in two thicknesses, 2.5 and 5 mm, and four Al alloy compositions with a nominally constant Mn content as detailed in Table I. These will be referred to as AM40, AM50, AM60, and AM70, respectively. The composition of the melt was determined by Optical Emissions Spectroscopy at Ford Research and Innovation Center, and will be referred to as the alloy composition. The target melt temperature was 948 K (675 °C). Sulfur hexafluoride, SF₆, was used as the cover gas to prevent oxidation.

Tensile specimens with a gage length of 25.4 mm and a width of 6.4 mm were machined from the as-cast plates in accordance to ASTM E8/B557. The specimen

thickness was equal to the plate thickness, 2.5 or 5 mm. Tensile testing was completed for 18 samples per condition, with nine tensile bars machined from each plate, at least 12 mm from the plate edge. Tensile testing was conducted on a hydraulic MTS load frame with a 25 mm extensometer at room temperature. Tests were conducted at an initial strain rate of $1 \times 10^{-3} \text{ s}^{-1}$, and a constant displacement rate of 2 mm/min until sample failure. These tests were used to analyze yield strength, ductility, and strain hardening exponent. Yield strength was calculated using the 0.2 pct offset method.

Metallographic samples were sectioned from the grip section of the tensile bars, and characterized for porosity, β -Mg₁₇Al₁₂, and grain size. Samples were prepared using standard techniques, with a final polish using 1 μm diamond paste. Buehler MetaDi fluid was used as a polishing lubricant in place of water. To characterize grain size, samples were etched for 3 seconds in a 278 K (5 °C) acetic nitric solution (5 mL nitric acid, 15 mL glacial acetic acid, 20 mL water, 60 mL ethanol).

Microhardness mapping was completed using an automated Vickers microhardness system with a load of 50 grams force and a dwell time of 13 seconds. Based on previous work by Yang *et al.*,^[26] in accordance with ASTM E384 standard, the spacing between measurements should be at least 2.5 times the length of the indentation diagonal. For these samples, indents were placed using a 100- μm spacing through the casting thickness.

The nominal area fraction of porosity was quantified using backscatter electron (BSE) SEM images. The nominal area fraction of porosity was determined using at least 10 images. The area fraction of β -Mg₁₇Al₁₂ was quantified using both image analysis of BSE SEM images and X-ray diffraction (XRD). β -Mg₁₇Al₁₂ phase fraction and distribution were quantified on the as-polished specimens. XRD was conducted on polished, through-thickness specimens placed in a Rigaku Rotating Anode X-ray Diffractometer.

Electron probe microanalysis (EPMA) was used to determine through-thickness composition. EPMA was performed using a Cameca SX-100 electron microprobe equipped with wavelength-dispersive spectrometers. The accelerating voltage and beam current were 15 kV and 10 nA, respectively. Standards of at least 99.9 pct pure Al, Mg, and Mn were used for calibration. Compositions are given as the average of at least 200-point measurements. Further details on the instrument settings and data analysis are reported in Berman *et al.*^[27]

Grain size was quantified through electron backscatter diffraction (EBSD). For EBSD orientation imaging maps, a step size of 0.5 μm and a scan area comprised of at least 1000 grains were used. The general digital image processing (cleaning) procedure applied to the maps was

Table I. Al and Mn Alloy Compositions for Each Condition as Measured by Optical Emission Spectroscopy

Composition	AM40	AM50	AM60	AM70
Al (wt pct)	3.8	4.6	6.0	7.0
Mn (wt pct)	0.55	0.4	0.44	0.44

(1) neighbor orientation correlation, (2) single iteration of grain dilation, and (3) grain confidence index (CI) standardization. After cleaning, only points with a $CI > 0.1$ were retained. Low confidence points appear black in the EBSD maps, indicating regions of secondary phases, grain boundaries, oxide films, or porosity. The minimum grain size retained after cleaning was set to $3 \mu\text{m}$ grain diameter. All experimental data, including tensile data and reference images, are archived for future use on the Materials Commons, an information repository maintained by the University of Michigan.^[28,29]

III. RESULTS AND DISCUSSION

A. Microstructural Characterization

The microstructure of the HPDC plates consists of fine, in-mold α -Mg cells (darker gray), large α -Mg ESCs, β -Mg₁₇Al₁₂ eutectic particles (light gray), and AlMn intermetallics (white), shown for each condition in Figure 1. The exact composition of the AlMn intermetallic phases is not determined in this work, but can be of the form Al₈Mn₅, AlMn₄, and Al₁₁Mn₄ as predicted by ThermoCalc using the TCMG4 database, and by previous work in AM series alloys.^[30,31] Examples of ESCs (large, dendritic structures in the core of the castings) are circled and shown in Figure 2, which is a cross-section of a cast plate in the etched condition. Shrinkage porosity can be observed approximately $600 \mu\text{m}$ from the casting surface. Microstructural characterization of in-mold grain size, ESC size, ESC area fraction, eutectic phase β -Mg₁₇Al₁₂, and casting defects was completed for all conditions, and in multiple regions through the thickness of the plates. Quantitative microstructural characteristics are tabulated in Table II, with the mean and standard deviation given for each characteristic.

1. Grain size

An important microstructural feature in die cast alloys is the variation in grain size that can be observed through the thickness of the casting. Grains are divided into two groups: grains that are formed in the die, termed in-mold α -Mg grains, and externally solidified grains or crystals (ESCs) that are formed in the shot sleeve before being injected into the die. Cast plates show two distinct regions, hereafter referred to as the skin and the core, shown in Figure 3, for (a) 2.5 mm AM50 and (b) 5 mm AM50. The skin is the fine-grained region adjacent to the casting surface, and the core is the bulk of the material in the center through thickness. To determine the average in-mold grain diameter, EBSD data were partitioned to include only grains less than $30 \mu\text{m}$ in diameter. The in-mold α -Mg grain size is independent of Al content and thickness, and averages between 12 to $20 \mu\text{m}$ in grain diameter as shown in Figure 4. The in-mold α -Mg grain size did not vary through the thickness; grains near the casting surface and in the core have the same average in-mold grain diameter. When comparing the in-mold grain size area

fraction histograms for all Al contents in the skin and core, the histograms have the same peak value and distribution. Thus, the in-mold grain size is considered the same for all plates.

The precise characteristics of ESCs are difficult to quantify and include solute (Al) content, fractal geometry, and size. Operationally in this investigation, ESCs were defined as α -Mg grains which are greater than $30 \mu\text{m}$ in diameter.^[32] ESC size can vary up to an order of magnitude, ranging from the operational minimum of $30 \mu\text{m}$ up to approximately $300 \mu\text{m}$ in diameter. The area average ESC size is approximately 50 to $80 \mu\text{m}$ in diameter. Values for the average ESC size and area fraction are given in Table II. The area average ESC size for all eight conditions is similar, despite the wide range of ESC sizes that were observed. The area fraction of ESCs did depend on location through the thickness, with a higher fraction observed in the core regions of the castings.

Based on the consistent in-mold and ESC grain sizes shown in Table II, the grain size data for all aluminum contents of each thickness are compiled into one dataset for each location (skin or core), and an area average in-mold grain size, ESC size, and area fraction for the skin and the core of each plate thickness is found. The area fraction grain size distribution for all grains in the skin and in the core is shown in Figure 5. Figure 5 shows that the area fraction of ESCs is higher in the core than in the skin. The ESCs in the core are surrounded by the fine in-mold α -Mg grains. The in-mold grain size in the core is slightly larger than in the skin, but the in-mold grains occupy a much smaller fraction of the area. The measured area fraction of ESCs in the core was determined to be approximately 45 pct of the area of the core, with values ranging from 30 to 60 pct of the area. This was the same for both the 2.5- and 5 mm-thick plates. Very few ESCs were observed in the near surface region in the 2.5 mm plates, but large grains (ESCs) were frequently observed in the near surface region of the 5 mm plates, leading to the weakened in-mold peak for the skin region of the 5 mm plates. A decrease in peak height is reflective of a decrease in the total area fraction of grains of a given size, in this case the in-mold grains in the skin of the 5 mm plates. This was dependent on sampling location along the edge of the casting, but typically ranged from 30 to 45 pct area fraction.

Using the through-thickness EBSD scans shown in Figure 3, the grain size data are partitioned into bins $50 \mu\text{m}$ wide. There is a homogeneous fine grain size observed in the skin region of the 2.5 mm plates. Grains greater than $30 \mu\text{m}$ in diameter first occur at a distance of approximately $600 \mu\text{m}$ from the casting surface in the 2.5 mm plates. The through-thickness microstructure in the 5 mm plates is more complex and there is significant plate-to-plate variability although casting conditions remained constant. The microstructure in the 5 mm-thick plates typically formed with three distinct bands of grains. Immediately beneath the casting surface, bands of large α -Mg grains were frequently observed. Adjacent to this layer, a region of fine grains,

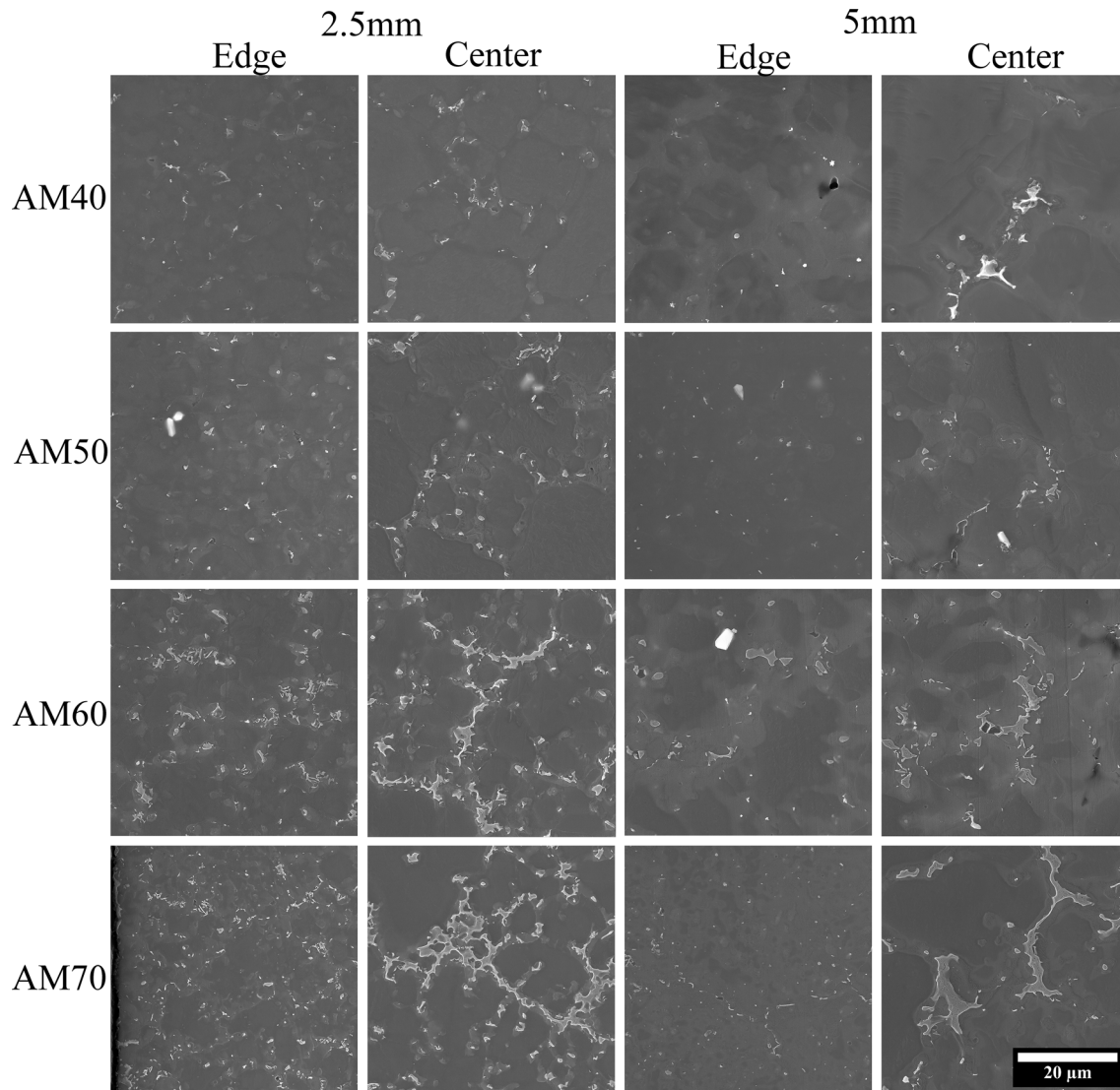


Fig. 1—The microstructure of the as-cast plates is comprised of fine α -Mg grains (darker gray), surrounded by β -Mg₁₇Al₁₂ eutectic particles (light gray), with randomly distributed Al₄Mn particles (white) for each condition.

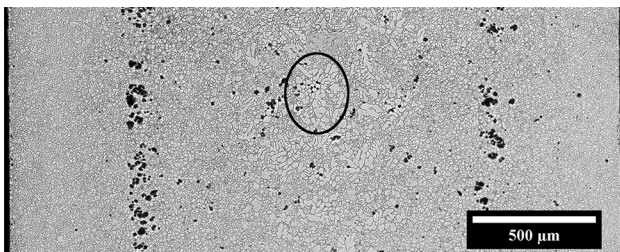


Fig. 2—Representative image of porosity through the thickness of the plate, where the left and right sides are the casting surface. Image is an optical micrograph of an AM50 2.5 mm-thick plate. Externally Solidified Crystals (ESCs) (an example is circled) are evident in the core of the plate. Also notable in this image are pore bands roughly 600 μ m from the casting surface.

and then in the core of the casting, ESCs were observed. An example of this is shown in Figure 3(b). The area fraction of grains greater than 30 μ m observed at the

surface was 20 pct for the 5 mm plates, while no ESCs were observed in skin of the 2.5 mm plates.

2. Factors affected by aluminum content

The aluminum and manganese content was quantitatively characterized in both the skin and core regions for all four alloys using EPMA. The skin content was measured in a region ~200 to 400 μ m from the casting surface and the core content was measured at mid-thickness. As the electron interaction volume is of comparable size (~4 μ m) to the in-mold grain diameter (12 to 20 μ m), it is difficult to isolate only the solute content of the matrix for the in-mold grains. For the purposes of this work, the concentration of solute in solid solution is approximated as the mean of all composition measurements. For this set of castings, it is observed that as the Al alloy composition increases, the Mn content of the solid solution decreased, as shown in Figure 6.

The primary eutectic phase in AM series alloys is the β -Mg₁₇Al₁₂ phase. The β -phase fraction was quantified

Table II. Microstructure Summary for Each of the Key Features, Including Area Average Grain Diameter for In-Mold Grains and ESCs, ESC Area Fraction, β -Phase Fraction, and Porosity Levels

	AM40 2.5 mm	AM50 2.5 mm	AM60 2.5 mm	AM70 2.5 mm	AM40 5 mm	AM50 5 mm	AM60 5 mm	AM70 5 mm
In-mold grain size skin (μm)	12 \pm 3	13 \pm 4	12 \pm 3	14 \pm 3	14 \pm 5	20 \pm 6	15 \pm 4	17 \pm 5
In-mold grain size core (μm)	16 \pm 4	18 \pm 5	16 \pm 5	17 \pm 5	18 \pm 5	17 \pm 5	17 \pm 5	16 \pm 5
ESC diameter core (μm)	79 \pm 24	70 \pm 21	66 \pm 18	58 \pm 15	64 \pm 18	71 \pm 22	78 \pm 24	75 \pm 23
ESC area fraction in skin (pct)	0	0	2	5	10	42	13	49
ESC area fraction in core (pct)	55	48	46	32	53	61	50	40
β SEM vol pct	1.4 \pm 0.3	1.4 \pm 0.3	3.3 \pm 1.0	4.9 \pm 0.9	0.5 \pm 0.1	0.8 \pm 0.1	1.4 \pm 0.3	2.4 \pm 0.4
β XRD vol pct	0.7	1.0	2.5	3.8	0.3	0.8	1.5	2.5
Porosity area (pct)	0.3	0.7	0.9	0.7	0.6	0.7	1.1	0.8

using both XRD and SEM. Using XRD, the overall β -Mg₁₇Al₁₂ phase fraction was determined by measuring relative peak intensity between the α - and β - phases. The intensity of the β -Mg₁₇Al₁₂ peaks increased with increasing Al in the alloy, indicating an increase in the phase fraction. The average (through-thickness) β -phase volume fraction measurements from SEM BSE image analysis were very similar values to XRD measurements as shown in Figure 7. As expected, increasing Al alloy content led to an increase in the amount of β -phase. Higher volume fractions of β -phase were measured in the 2.5 mm plates when compared to the 5 mm plates as shown in Figure 7 and in Table II. The amount of β -phase, as measured using BSE imaging, was observed to vary through the thickness of the plate. The skin is observed to have a higher β -phase fraction than the core, and this effect is pronounced in the 2.5 mm-thick castings. In the 5 mm plates, there is minimal variation in the volume fraction of β -phase as a function of through-thickness location. In contrast, in the 2.5 mm-thick plates for the alloys containing higher Al contents a significant change in the β -phase was observed depending on the through-thickness location with a maximum β -phase fraction observed approximately 250 μm from the casting surface.

Coincident with the through-thickness variation in the volume fraction of β -phase, there is also a change in the particle shape and degree of interconnection of the β -phase. Isolated β -phase particles are found in both the skin and core regions of the AM40 plates (Figure 1). As the alloy Al concentration increases, the volume of point particles in the skin increases and the β -phase in the core region becomes increasingly interconnected. This is shown in Figure 1, where the β -phase network in the core of the 2.5 mm-thick AM70 forms a more complete network than in that of the AM40 2.5 mm core. This trend is similar in the 5 mm-thick plates, although the frequency of the larger, networked β -phase particles is lower due to the lower overall volume fraction of β -phase observed.

3. Shrinkage porosity

In addition to externally solidified grains, other extrinsic microstructural features were observed, specifically, pores, pore bands, and oxide films. The SVDC process used for casting in this study reduced the amount of porosity within the plates compared to that

generally observed in high-pressure die castings.^[32] The microporosity that was observed was typically shrinkage porosity, with minimal gas entrapment, as observed in Figure 2. Typical levels of porosity measured on polished surfaces were less than 2 pct area fraction, independent of Al content (Figure 8). The shrinkage porosity was frequently observed in a “defect band” structure that was highly variable from casting to casting and location to location.

Typical of the chaotic molten metal flow produced by HPDC, defect bands occurred in many, but not all, of the castings. If present, they were observed approximately 500 μm from the surface of the casting in the 2.5 mm plates, and between 1000 and 2000 μm from the surface in the 5 mm plates. The defect bands varied in width, and while there was no discernable band structure in some samples, there were multiple bands in others. This is comparable to previous work by Gourlay *et al.*, where defect band appearance varied from casting to casting.^[33] Oxide films were also observed in many castings. There was a wide range of oxide sizes observed, from approximately 30 to 100 μm ; however, they were not quantified in this study.

B. Mechanical Behavior

1. Hardness testing

The through-thickness spatial variation in microhardness was measured for the 4 and 7 wt pct Al in both the 2.5 and 5 mm plates. The resulting microhardness maps are shown in Figure 9. Porosity bands are observed in subsurface in the 5 mm plates in Figures 9(c) and (d). Automated regular measurement grids were used with a spacing of 100 μm . Locations with a measured hardness above 100 Vickers hardness were locations where indents were placed on either oxide films or large AlMn intermetallic particles. The formation of a high-hardness skin region was observed in the 2.5 mm plates. This skin is approximately 600 μm thick. This is consistent with the first observance of ESCs at approximately 600 μm subsurface as observed in the 2.5 mm plates. In the 5 mm plates, the thickness of the higher hardness skin was somewhat variable, but had a nominal thickness of approximately 1100 μm . Defect bands were observed in the core regions of the 5 mm plates, and some regions of higher hardness in the core. This is consistent with the grain size distributions observed, as the formation of

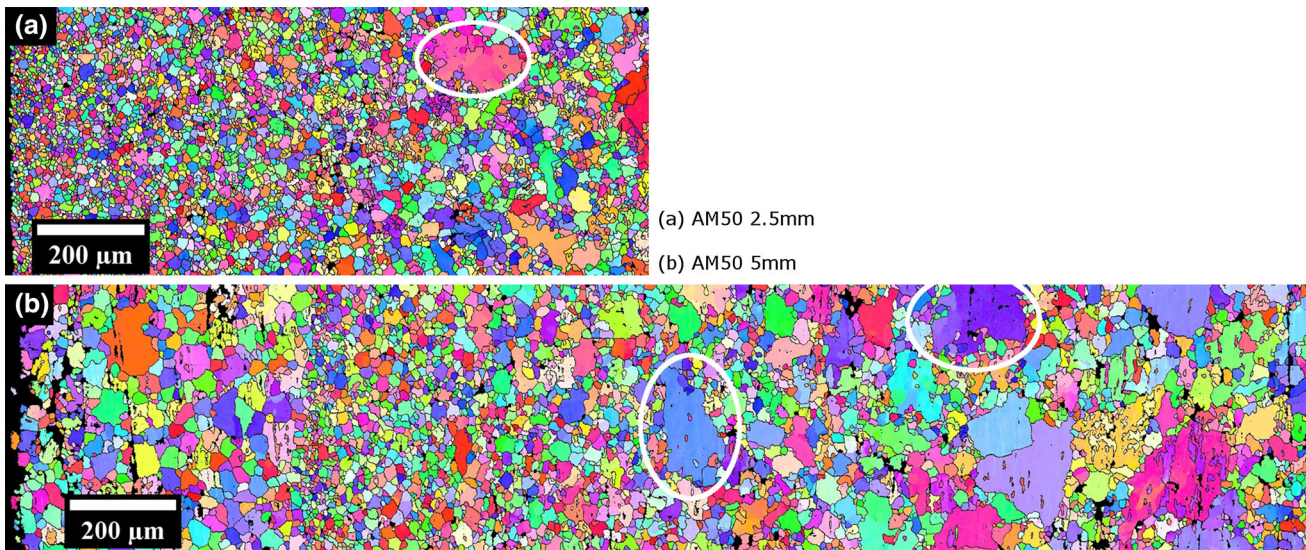


Fig. 3—Through-thickness microstructural variation as characterized using EBSD for (a) 2.5 mm plate, (b) 5 mm plate. Note white circles showing large grains associated with externally solidified crystals (ESCs). The as-cast plate surface is on the left of the images.

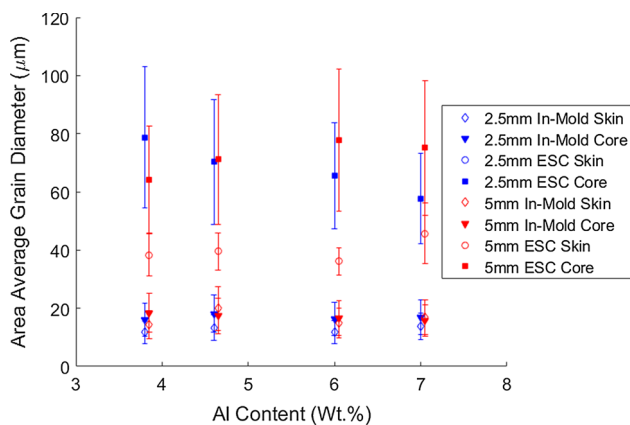


Fig. 4—Area average grain diameter for in-mold α -Mg grains and externally solidified crystals (ESCs) from each condition and location. Note that ESCs are substantially larger than in-mold grains.

large grains was also observed in the skin regions of the 5 mm plates.

2. Tensile testing

Representative tensile curves for each of the eight conditions of the as-cast plates are shown in Figure 10. Table III summarizes the tensile properties for each condition, including the average and standard deviation for each property. In general, with increasing Al content, an increase in yield strength and a decrease in ductility, fracture strength, and strain hardening exponent were observed as shown in Figures 11 and 12.

In Figure 11(a), yield strength was observed to increase linearly with increasing Al content of the alloys. As the Al content increases from 3.8 to 7 wt. pct, there is an increase in yield strength from 109 to 127 MPa and from 81 to 105 MPa in the 2.5- and 5.0 mm-thick plates, respectively. This is an increase in yield strength of 16.5 pct for the 2.5 mm-thick plates and 29.6 pct for the 5.0 mm-thick plates. The yield

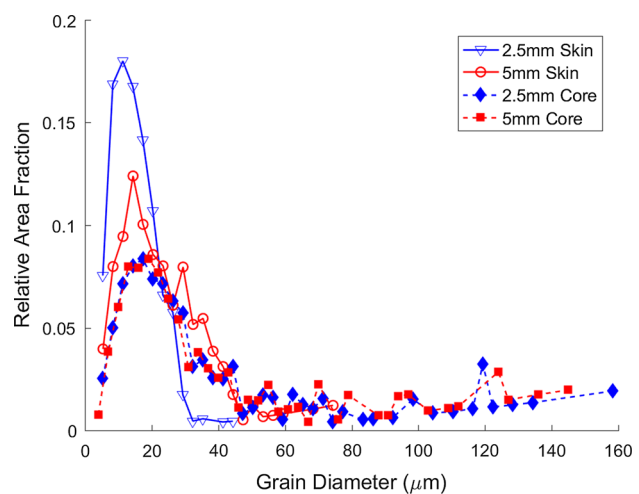


Fig. 5—Area fraction histogram for the grain size in the skin (solid) and the core (dashed). Large grains are observed in both regions of the 5 mm-thick plates.

strength of the 5 mm plates was consistently between 20 and 30 MPa lower than in the 2.5 mm plates.

Elongation to failure tended to decrease with increasing Al content and thickness, Figure 11(b). The elongation to failure between the least and most ductile specimens ranged up to 11 pct within a single condition. The highest value was 18.4 pct for the AM40 2.5 mm-thick plates, the lowest value was 3.1 pct for the AM70 2.5 mm-thick plates. Overall, the 2.5 mm plates tended to have higher ductility, although the ductility was similar for both plate thicknesses of AM70.

The samples did not exhibit necking, so the strength at fracture is determined rather than the ultimate tensile strength. It appears that fracture strength of the 5 mm plate castings is weakly dependent on Al content as shown in Figure 11(a). The 5 mm plates have a slightly lower fracture strength than the 2.5 mm plates. Compared with the yield strength, substantially more

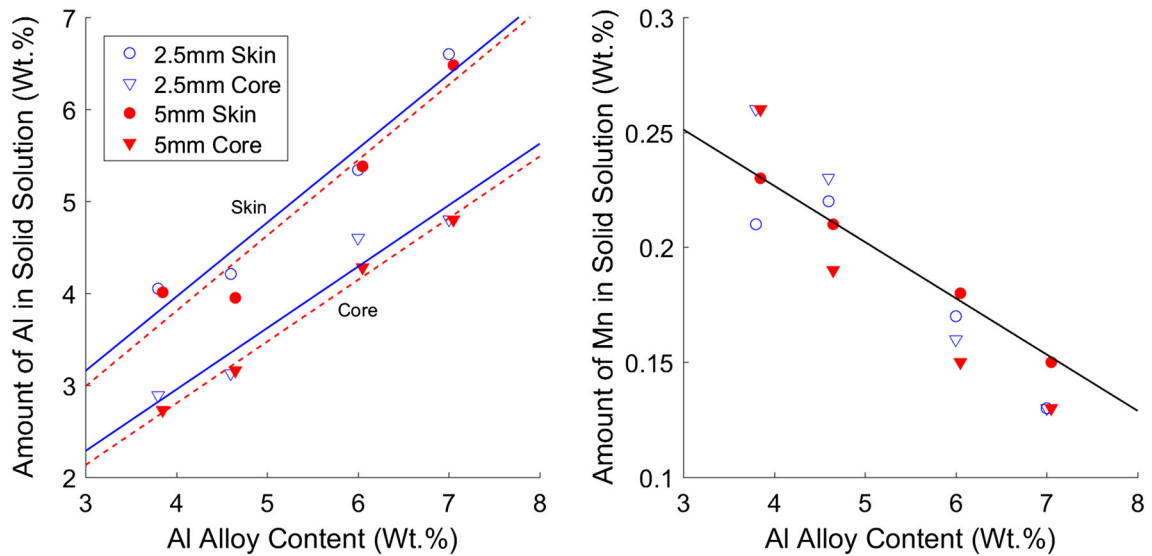


Fig. 6—Local composition measured by EPMA. As alloy Al content increases, the amount of Al which remains in solid solution increases, while the Mn fraction in solid solution decreases. The amount of Al in solid solution is higher in the skin than in the core, and is consistent for both plate thicknesses. The 2.5 mm data is shown using solid lines, and 5 mm using dashed lines. There is no change in the Mn in solid solution, shown by a single solid line for both plate thicknesses and location through-thickness.

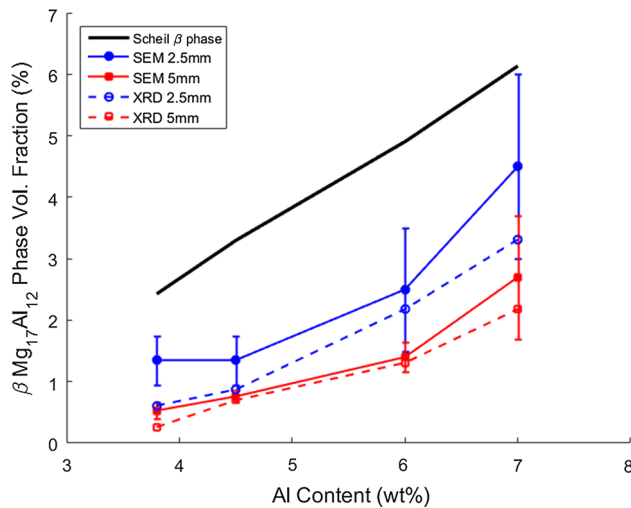


Fig. 7— β -phase volume fraction vs. alloy Al content as measured by SEM (closed symbols) and XRD peak fitting (open symbols). The Scheil curve is a theoretical curve for the β -phase fraction predicted under Scheil solidification conditions using ThermoCalc.

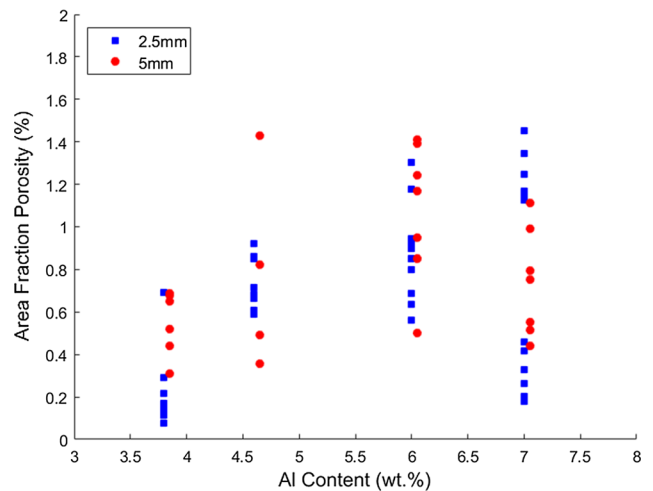


Fig. 8—Area fraction of porosity measured from at least 5 locations for each condition using SEM back-scattered electron (BSE) imaging. There is no statistically significant observable dependence of porosity on Al content or thickness.

variability was observed for the fracture strength. The ranges observed in fracture strengths are likely tied to the variation in overall elongation as discussed above.

Strain hardening exponent can be calculated using various constitutive relationships. Two common methods of calculation, the Hollomon (Eq. [1]) and Ludwik (Eq. [2]) empirical models, were used to quantify the influence of Al content and plate thickness on work hardening. The strain hardening exponent, n_1 , and strength coefficient, K_1 , are found from a true stress—true strain curve for both equations. The Ludwik strain hardening parameters tend to be higher values than those determined using the Hollomon relationship. Consistent with the findings for yield strength, the

strength coefficient, K , tends to increase with increasing Al content, while the strain hardening exponent decreases. The strain hardening exponents in Table III are comparable to those measured at a similar strain rate in AZ series Mg alloys.^[34]

$$\sigma = K\epsilon^n \quad [1]$$

$$\sigma = \sigma_Y + K_1\epsilon^{n_1} \quad [2]$$

Within a single casting, variability of properties can be significant due to the stochastic nature of microstructures present in high-pressure die castings. These large data populations allowed quantification of the statistical

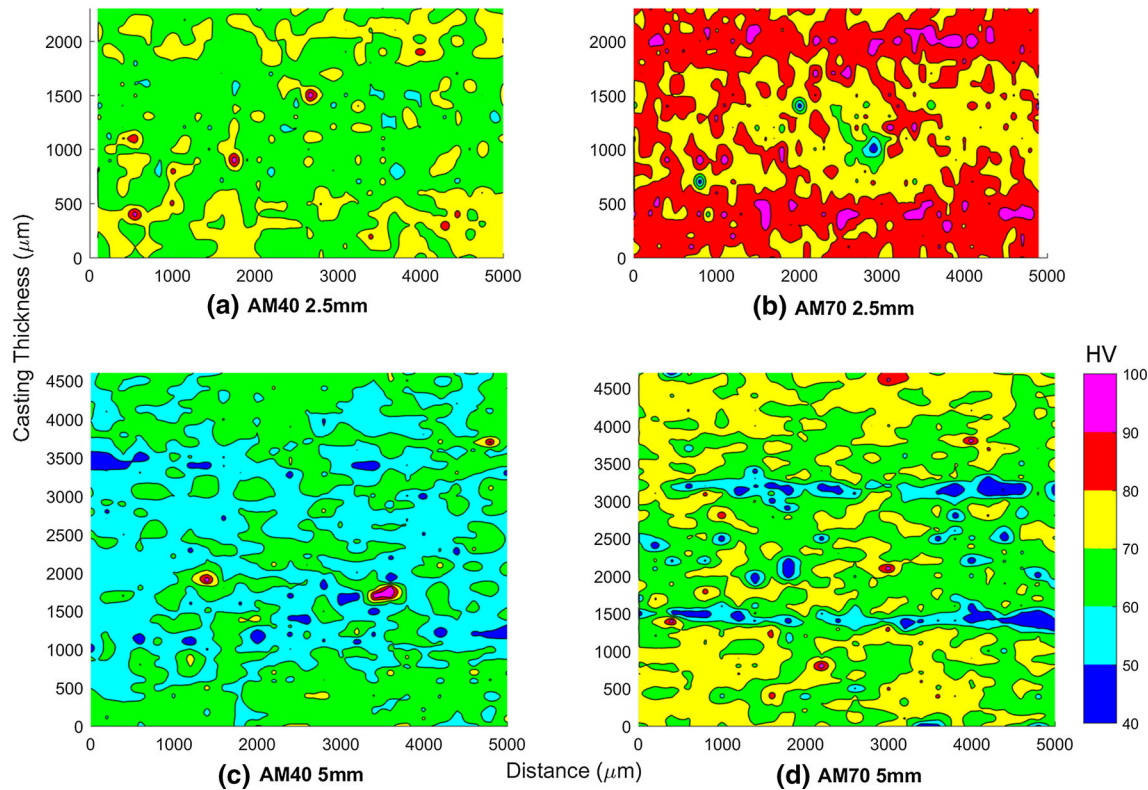


Fig. 9—Map of Vickers microhardness through the sample thickness for (a) AM40 2.5 mm, (b) AM70 2.5 mm, (c) AM40 5 mm, and (d) AM70 5 mm.

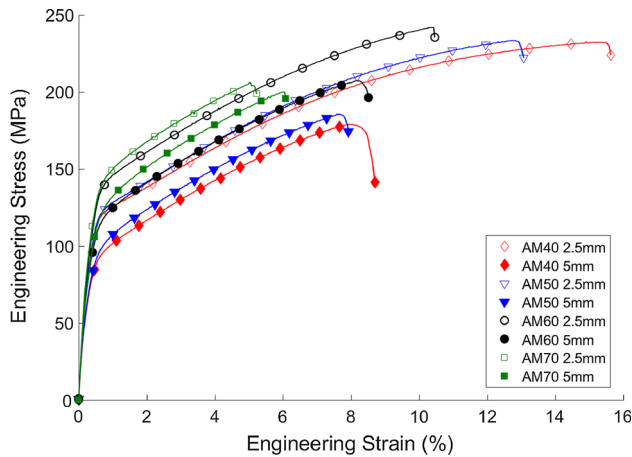


Fig. 10—Representative tensile curves from each of the eight experimental conditions. 2.5 mm plates are shown using open symbols, and the 5 mm plates are shown using filled symbols.

significance of the observed differences in the mean and standard deviation, as well as the level of significance of the scatter using the coefficient of variation (COV). Using an analysis of variance (ANOVA), the statistical significance of the differences depicted in Figures 11 and 12 could be determined. For this purpose, a 2×4 factorial ANOVA was conducted using the open source software, R, which incorporated any random effects for each material property within a given plate. Based on this ANOVA, the observed effects (or lack of effects) of

aluminum content and sample thickness on the tensile properties were determined to be statistically significant differences except for the 2.5 mm AM40 and AM50 conditions. These conditions could not be statistically proven to be different populations; however, their behavior was consistent with the overall trends shown in Figure 11.

To quantitatively assess the variability between properties, the COV was calculated for each property and is listed in Table IV. The COV is found by dividing the standard deviation by the mean, and is a measure of the overall variability of a set of samples, independent of typical sample means or measurement units, so that we can compare variability between properties. A sample set with no variation in the mean has a COV of zero, while a COV greater than 10 indicates that the sample set has a high degree of variability or dispersion in the dataset.

Overall, there was minimal scatter in the yield strength values for a given condition, with a maximum sample-to-sample scatter of 12 MPa for AM70 in the 2.5 mm plate condition. The yield strength COV was consistently low, between 1 and 3. In contrast, ductility had much higher variability with a maximum range of 11 pct elongation for a single condition. The COV for elongation to failure was particularly high, with a maximum of 24.5, which is typical for ductility in cast materials.^[32] It is common to see outliers in the distribution of elongations for a given condition. These outliers are more than 1.5 times the standard deviation. Qualitative fractography reveals that the outlier samples

Table III. Tensile Property Summary—Mean ± Standard Deviation for the Yield Strength, Total Elongation to Failure, Fracture Strength, and Strain Hardening Parameters (Hollomon and Ludwik) for Each Condition

	AM40 2.5 mm	AM50 2.5 mm	AM60 2.5 mm	AM70 2.5 mm	AM40 5 mm	AM50 5 mm	AM60 5 mm	AM70 5 mm
Yield strength (MPa)	107 ± 2	109 ± 2	120 ± 3	127 ± 3	82 ± 2	87 ± 2	102 ± 3	105 ± 1
Elongation (pct)	14.4 ± 2.9	13.3 ± 2.4	10.5 ± 2.2	5.1 ± 1.1	9.6 ± 2.3	7.5 ± 1.5	8.3 ± 1.4	6.2 ± 1.0
Fracture strength (MPa)	229 ± 9	233 ± 12	241 ± 10	208 ± 12	185 ± 18	180 ± 15	209 ± 11	197 ± 11
n Hollomon	.35 ± .002	.354 ± .01	.321 ± .01	.26 ± .02	.38 ± .03	.35 ± .02	.34 ± .01	.30 ± .01
K Hollomon	543 ± 6	558 ± 19	558 ± 13	475 ± 28	512 ± 52	491 ± 36	528 ± 21	489 ± 27
n_1 Ludwik	.81 ± .04	.81 ± .03	.77 ± .04	.75 ± .03	.81 ± .04	.80 ± .02	.78 ± .03	.72 ± .01
K_1 Ludwik	877 ± 105	915 ± 88	900 ± 74	883 ± 45	912 ± 100	909 ± 38	921 ± 54	830 ± 25

with low ductility typically have a large defect on the fracture surface, either an oxide film or porosity. Figure 11(b) shows the range of ductility observed for each condition. The COV for fracture strength and the Hollomon strain hardening exponent indicated that these properties were reasonably well behaved, exhibiting values that were low to moderate, as shown in Table IV.

IV. DISCUSSION

A. Microstructure discussion

Quantitative characterization of microstructural features has been limited in previous research on HPDC AM series alloys, and thus a major contribution of the current study is the quantitative microstructural information coupled with statistically significant mechanical behavior datasets.

In-mold and ESC grains are the major microstructural features which are dependent on the through-thickness location. In-mold grain size was found to be independent of Al content and plate thickness. This is consistent with previous observations made by Bowles *et al.*^[35] The in-mold grain size is very fine immediately adjacent to the casting surface in the 2.5 mm plates, but this rapidly cooled region is only 10 to 25 μm thick. The grain size quantified in the current study is comparable with that reported in HPDC binary Mg-Al alloys in other studies.^[35,36] By thresholding the data used to calculate the grain diameter for in-mold grains and ESCs separately, the in-mold grain size can be better defined. A similar fraction of ESCs was observed in both the 2.5 and 5 mm-thick plates. ESC size and distribution have been shown previously to vary based on the HPDC gating systems, but plates in this study had gate inlets that were unrestricted (*e.g.*, they were similar in thickness to the plate thickness). In addition, metallographic samples were taken from the same location in each plate in order to minimize any location effects.^[37] Variation in the ESC fraction is likely a random effect due to variation within the casting parameters and sampling, leading to range in ESC fraction from 30 to 60 pct. This is similar to the range of ESC fractions observed by Laukli.^[38]

The die cast skin region can have an important influence on tensile properties.^[13,32,39] There are a

number of methods which have previously been used to define the skin thickness—defect band distance, microhardness, grain size variation, and microplasticity analysis.^[33,39–41] In the current research, the skin was somewhat difficult to quantify. The transition from skin to core regions is defined using a combination of an increase in the area average grain diameter above 30 μm , and a decrease in the hardness in the core regions. Operationally, the skin was determined to be the region from the casting surface to approximately 600 μm in depth in the 2.5 mm plates based on grain size and microhardness mapping. However, the 5 mm plates did not show a consistent change in grain size and generally have a slightly larger grain size than the 2.5 mm plates. There is a higher and somewhat variable hardness band which is approximately 1100 μm thick.

Microhardness mapping has shown that the skin layer is non-uniform through a casting, and that the difference in hardness increases between skin and core with Al content.^[16,26] Microhardness mapping is utilized in this study in order to validate the skin thickness obtained from the average grain size. Microhardness results correspond well with previous work by Yang *et al.* for the 2.5 mm plates. In the 5 mm plates, the hardness is slightly higher in the skin than the core, and there is a significant decrease shown around defect bands. The overall hardness in the 5 mm plates is lower than in the 2.5 mm plates, likely due to the larger area average grain size through the thickness.

As expected for the non-equilibrium solidification conditions present in high-pressure die castings, as the Al content increased, the β -phase volume fraction also increased.^[42,43] As sample thickness increased, the amount of β -phase decreased, similar to behavior observed by Cáceres.^[19] Total β -phase fraction through thickness as measured by XRD correlates well to previous work by Barbagallo.^[44] In addition, the shape and distribution of the β -phase eutectics changed as a function of distance from the surface, as previously observed in AZ91.^[45] For AM40 and AM50, the β -phase is in the form of point particles through the full thickness. In AM60 and AM70, interconnected networks begin to form and increase in size with aluminum content. This change in β -phase structure was much stronger in the 2.5 mm plates than the 5 mm plates, similar to the grain size behavior.

The high cooling rates associated with high-pressure die casting are not at equilibrium and lead to the

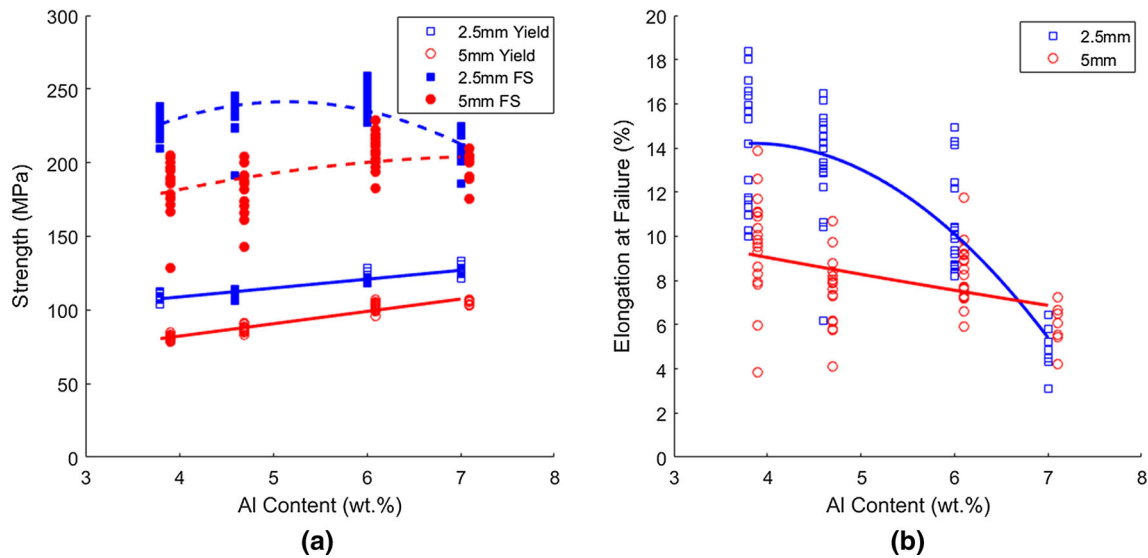


Fig. 11—(a) Yield strength (solid line) increases with Al content for both the 2.5 and 5 mm plates. Fracture strength (dashed line) increases with aluminum content, and then decreases as elongation significantly decreases. (b) Elongation decreases with increasing Al content. The effect of aluminum content is more pronounced in the 2.5 mm plates.

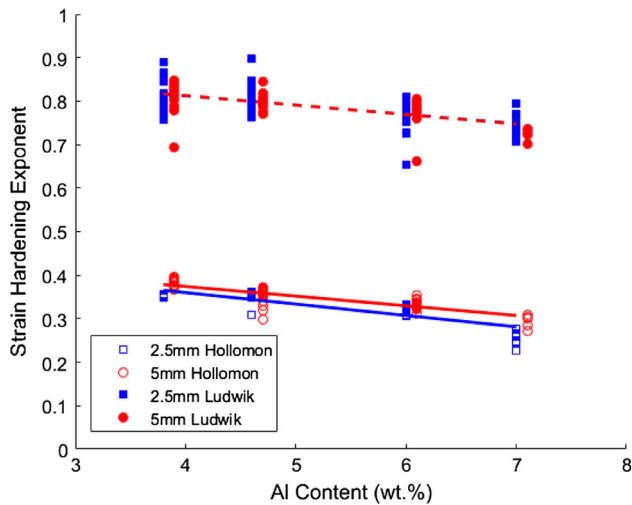


Fig. 12—Strain hardening exponent decreases for both Ludwik (dashed line) and Hollomon (solid line) constitutive relationships.

partitioning of Al from the center of the α -Mg grains into the grain edges. This produces coring of the α -Mg cells, with a low Al content core to an Al-rich solid solution at the edges. Scheil solidification conditions are often used to model the microstructural development in non-equilibrium cooling,^[46] although it is not clear

whether this is appropriate for the solidification conditions present in HPDC or SVDC.^[47] Scheil–Gulliver solidification assumes no diffusion in the solid phases, no concentration gradients in the liquid, and that equilibrium exists at the interface. In this investigation, the β -Mg₁₇Al₁₂ phase fraction was computed assuming Scheil solidification conditions using ThermoCalc, with the TCMG4 database, with the results shown in Figure 7. The amount of β -phase overall through the casting thickness can be compared to that predicted by the Scheil solidification model,^[46] and is lower than expected.

The plate castings used in this study were produced using SVDC, and thus the porosity levels in these plates were significantly lower than that observed for typical HPDC components. This is consistent with previous observations in AZ91 that application of very high vacuum pressures results in lower levels of porosity.^[48,49] In the current study, porosity levels were determined to be independent of Al content and thickness. Although some previous work has suggested that porosity increases with increasing plate thickness, this is not always the case.^[20,50] In the current study, porosity was observed in the core of the plates, between dendrite arms of ESCs, which is similar to recent work by Li *et al.*, where shrinkage porosity was imaged using X-ray tomography on a HPDC AM60 sample.^[51] The defect

Table IV. Tensile Property Coefficient of Variation for the Yield Strength, Total Elongation, Fracture Strength, and the Hollomon Strain Hardening Exponent for Each Condition

COV (pct)	AM40 2.5 mm	AM50 2.5 mm	AM60 2.5 mm	AM70 2.5 mm	AM40 5 mm	AM50 5 mm	AM60 5 mm	AM70 5 mm
Yield	1.9	2.1	2.7	2.5	2.3	2.7	2.5	1.3
Elongation	19.9	18.1	20.7	21.1	24.5	20.5	16.3	15.6
Fracture strength	3.7	5.0	4.3	5.8	9.6	8.2	5.4	5.7
<i>n</i> Hollomon	0.6	3.3	2.5	6.3	8.8	5.7	3.3	5.0

Table V. Model Coefficients from Current Work and Previous Work

Model	Material	σ_0 (MPa)	K_y (MPa m ^{1/2} at. ⁻¹)	B_{Al} (MPa at. ⁻ⁿ)	f_{skin} (Sample Thickness)
Current Work	AM40-AM70	4.5	0.21 + 2.75(X_{Al})	20, $n = 1/2$	0.45 (2.5 and 5 mm)
Sharifi ^[17,80]	AM60	62.1	0.153	—	0.30 (2.6 mm)
Toda ^[18]	Mg alloys	10	0.21 + 2(X_{Al})	26.7, $n = 2/3$	—
Yang ^[16]	Mg-Al	12	0.22 to 0.30	21.2, $n = 1/2$ 39.5, $n = 2/3$ ^[71,83]	0.10 (3 mm)

band structure observed for all conditions is similar to that observed by Laukli in AM60, forming approximately 1000 to 2000 μm from the casting surface in the 5 mm plates.^[37] The defect bands are not present in all castings.^[33,52] There is no consistent effect of Al content or thickness on the formation of defect bands, which is consistent with previous observations. Similarly, some macro-segregation of Al was observed in the near surface regions, comparable to that observed by Lee *et al.*^[53] This occurs in less than 1 pct of the area observed and is not considered significant.

B. Tensile Properties

With increasing Al content, there is an increase in yield strength and decrease in ductility, strain hardening exponent, and hardening coefficient. This is consistent with prior work from Aune *et al.* and Dargusch *et al.*^[21,54,55] The general trend of increasing yield strength with Al content is explored in detail in the following section. The reduction in ductility with Al content could be attributed to a number of different factors, in particular, to the increased strengthening from increased Al solute content, increasing β -phase fraction, or shrinkage porosity, which leads to local cracks in the microstructure. Further study is needed to identify the dominant final fracture mechanisms in these SVDC alloys. The strain hardening exponent is a measure of the capability of a metal to deform before fracture. The decrease in strain hardening exponent reflects the decreased hardening capacity in the higher aluminum content alloys. This is comparable to previous work by Tahreen in the AZ series.^[56] The Ludwik strain hardening exponent is computed in order to compare with previous work by Cheng *et al.* to determine material properties for use in a FEA model.^[57]

With increased section thickness, lower yield strength and ductility is observed. This is consistent with previous observations by a number of researchers.^[19,20,54,58–60] Aghion *et al.* attribute the decreased yield strength with increased thickness to the increase in solidification time, and in turn the increased grain size.^[58] However, average grain size is only slightly larger in the 5 mm plates for the current results. Instead, we attribute this decrease to the increased grain size on the surface of the casting compared with the surface regions of the 2.5 mm-thick castings, and the increased ESC fraction, which significantly reduces the effect of grain boundary strengthening. This is further explored in the model development section below.

C. Yield Strength Model

By using measured microstructural features as input, physics-based models for yield strength can be developed. In general, linear superposition methods have been used to predict the contributions to yield strength from different strengthening mechanisms.^[61–63] There are three primary strengthening mechanisms active for HPDC Mg alloys. These mechanisms are grain boundary, σ_{gb} , solid solution, σ_{ss} , and, so-called, “dispersion” strengthening, σ_{disp} .^[19,64] The overall strength can be predicted using linear superposition for these three mechanisms as shown in Eq. [3].^[16,65]

$$\sigma_y = \sigma_{gb} + \sigma_{ss} + \sigma_{disp} \quad [3]$$

Recent approaches to this linear superposition of mechanisms for cast Mg alloys have been proposed by Sharifi *et al.*, Toda-Carabello *et al.*, and Yang *et al.*^[16–18] These three models have been developed for use in multiple cast Mg alloys, including binary Mg-Al, AM60, and the AZ series. The key differences between each of these models are in the method of calculating each strengthening component, and the ability to extend to other major alloying elements, and the manner in which they deal with microstructural inhomogeneities that are commonly observed in HPDC materials. Using these models as a starting point, we have developed a linear superposition model that accounts for the three primary strengthening mechanisms, and also deals with microstructural inhomogeneities (skin and core) and the bimodal nature (in-mold grains vs ESCs) of HPDC microstructures. For a given region of the casting, σ_y is determined using the linear superposition model (Eq. [3]), with the relevant parameters given for the specific alloy/region under consideration. The manner of dealing with the specific mechanisms is described below.

The strengthening components used in Eq. [3] are calculated for each region of uniform microstructure in the casting, specifically the skin and the core regions. By taking these regions of uniform microstructure into account, the yield strength can be estimated using a weighted or composite model as suggested by Yang, in Eq. [4].^[16] For the castings investigated in this study, the fraction of material that is the skin, f_{skin} , is found by doubling the measured skin thickness, and dividing by the total plate thickness. As previously described, using hardness mapping and the presence of ESCs, the skin thickness could be estimated to be 600 μm thick in the 2.5 mm plates and 1100 μm thick in the 5 mm plates. In more complex castings, it is also likely related to the

molten metal flow patterns and cooling rate variation.^[66] Thus, the skin fraction, f_{skin} , observed in this study is 0.45 for both the 2.5 mm plates and the 5 mm plates. Within both the skin and core regions, the specific microstructural features and strengthening elements are individually accounted for in our calculations.

$$\sigma_{y_{\text{total}}} = f_{\text{skin}}\sigma_{y_{\text{skin}}} + (1 - f_{\text{skin}})\sigma_{y_{\text{core}}} \quad [4]$$

The solid solution strengthening term, σ_{ss} , accounts for strengthening due to solute atoms impeding dislocation motion, and is a function of the elastic and size misfits between solute and matrix atoms. In the AM series alloys investigated here, solute strengthening arises from both Al and Mn in a Mg solid solution. We account for solid solution strengthening based on a first principles model developed by Yasi *et al.*^[68] The influence of solute elements on the critical resolved shear stress for dislocation motion on the basal plane has been modeled by Yasi *et al.* using density functional theory.^[67] Yasi *et al.* assume a dilute concentration, weak obstacle Fleischer approach for predicting the force necessary to move a dislocation and overcome solute drag.^[68] This is given as a function of the atomic solute fraction, c , and a potency factor, M . The potency factor of Al and Mn was calculated by Yasi *et al.* as $M_{\text{Al}} = 19.6$ MPa and $M_{\text{Mn}} = 120.8$ MPa.^[67] In order to determine the yield strength contribution from solid solution strengthening, the critical resolved shear stress is multiplied by the Taylor factor, m . A Taylor factor of 4.5 is used in this work, as calculated for pure, polycrystalline Mg with random texture.^[69,70] The random texture is consistent with the HPDC materials investigated in this study. The atomic fraction of Al and Mn in solid solution in the skin and the core determined using EPMA provides the value for c_x in Eq. [5].

$$\sigma_{\text{SS}} = m * \sum M_x c_x^{\frac{1}{2}} \quad [5]$$

It is observed that for the particular alloys investigated in this study, as the amount of Al in solid solution within the α -Mg grains increases, the amount of Mn in solid solution was observed to decrease (Figure 6). Mn is known to be a very strong strengthening agent,^[68] however, since the fraction of Mn in solid solution decreases with increasing Al content, there is also a decrease in Mn solid solution strengthening at higher Al contents for the conditions investigated. The net result is that the combined solid solution strengthening from both Al and Mn remains constant over the range of Mg-Al-Mn alloys investigated. These results can be compared to previous work by Toda-Carabello and Caceres, who predict solid solution strengthening using the Labusch model, with an experimental fitting parameter.^[18,71] Both the Fleischer ($n = 1/2$) and Labusch ($n = 2/3$) models show similar and good agreement with solid solution strengthening in dilute Mg-Al alloys.^[71] The amount of strengthening predicted for Al in solid solution is essentially equivalent for all of these models, as shown in Table V, after adjusting for

the Taylor factor. However, we prefer the approach provided by Yasi *et al.* since it also includes well-defined solid solution strengthening parameters for all alloying elements in Mg, and thus can be readily extended to other alloys.

In the present case, minimal variation in solid solution strengthening is predicted to occur between the skin and core of the plates. The skin has a higher fraction Al in solid solution than in the core, likely due to the high cooling rate. In addition, the core has a higher fraction of ESCs, which tend to have a lower Al solute content.^[16] The solid solution strengthening component in the core consists of an average solute content for both the in-mold grains and ESCs due to measurement limitations. However, this change in Al is less than 1.5 wt pct Al, even in the most concentrated alloys. While this is a measurable change, it has a relatively modest effect on solid solution strengthening. Since the solute variation through thickness is the same in both the 2.5 and the 5 mm plates, this factor does not appear to be responsible for the decreased yield strength in the 5 mm plates.

The influence of grain size on yield strength is given by the Hall–Petch relationship in Eq. [6].^[72,73] The intrinsic stress term σ_0 in Eq. [6] is taken to be the CRSS of pure Mg with no influence of solute content. The intrinsic stress, σ_0 , is taken to be 4.5 MPa for all regions of the castings. This is based on single-crystal studies of the CRSS of Mg, which typically find a value of 0.7 to 1 MPa, and using the Taylor factor of 4.5.^[74–77] Previous work has used a CRSS of 12 MPa, determined from extruded Mg, but this is expected to be lower for cast magnesium alloys which have random grain orientations.^[78,79]

Alloying has also been shown to affect the Hall–Petch parameters, specifically the locking parameter, k_y .^[71,79,80] Different mechanistic rationales from this have been given, varying from changes in shear modulus with solute content^[18] to changes in slip transfer across or nucleation at grain boundaries.^[66] The influence of solute on the Hall–Petch locking parameter is considered separately from the matrix solid solution strengthening component described above. Toda-Carabello *et al.* proposed that the influence of solute elements on k_y follows the form given in Eq. [7], in which k_y is linearly proportional to the solute concentration multiplied by the proportion of the locking parameter that is attributable to a specific element, $\Delta k_{y,x}$. As shown in Eq. [7], this is then added to the locking parameter determined for pure Mg, $K_{y,\text{mg}}$. In the current work, we estimate the locking parameter, k_y , to vary from 0.27 to 0.33 MPa $\mu\text{m}^{1/2}$, depending on alloy composition. This was determined empirically by fitting the grain boundary component of the yield strength to the influence of solute content in Eq. [7].^[16,18] The locking parameter associated with pure Mg, $k_{y,\text{Mg}}$, has been determined to be 0.21 to 0.22.^[78,79] We have used a value of 0.21 in the current work. We conducted a linear regression for $\Delta k_{y,\text{Al}}$ to account for the influence of Al on the grain boundary strengthening, accounting for Al in atomic fraction, c_x .

In this case, $k_{y,Al}$ is calculated to be 2.75 in these alloys using the area average in-mold and ESC grain sizes described in Section III-A-1. Due to the low solubility of Mn in Mg and that it is nominally constant for the four alloys investigated, we assume that the effect of Mn on k_y is negligible and $\Delta k_{y,Mn} = 0$. Further work is needed to determine if this assumption is valid.

$$\sigma_{gb} = \sigma_0 + k_y * d^{-\frac{1}{2}} \quad [6]$$

$$k_y = k_{y,Mg} + \sum c_x \Delta k_{y,x} \quad [7]$$

The grain size effect on strength is further complicated by the presence of the fine-grained skin and the relatively coarse-grained core regions. In addition, within each of these regions there are often two types and sizes of grains, fine, in-mold grains and coarser ESCs. To account for this, we used a bivariate grain size distribution to estimate the strengthening effects of the in-mold grains and the ESCs using Eq. [8].^[81] This allows for estimating the influence of ESCs which, due to their low frequency, only slightly increase the number average, but which can occupy up to 50 pct of the area in the core of the castings, significantly reducing the overall strengthening effect. In addition to being coarser, ESCs are thought to be areas of low Al content;^[36] however, this effect is not considered in the current study.

$$\sigma_{gb} = \sigma_0 + f_{ESC} * \left(k_y * d_{ESC}^{-\frac{1}{2}} \right) + (1 - f_{ESC}) * \left(k_y * d_{in-mold}^{-\frac{1}{2}} \right) \quad [8]$$

The 5 mm plates exhibited lower yield strengths in all of the alloys studied. The observation could be understood by accounting for the increased grain size in the skin region of the 5 mm-thick samples compared to the 2.5 mm-thick samples. This leads to a reduction in the strengthening effects attributed to the die-cast surface skin. When these factors were considered in the weighted model, a good estimate of the strength of all conditions was achieved.

The final strengthening mechanism in the linear superposition model is so-called “dispersion” strengthening which occurs as a result of the β -Mg₁₇Al₁₂ particles in the material.^[19] Since these particles are very coarse, strengthening occurs primarily through stress redistribution that occurs due to the modulus difference between the β -Mg₁₇Al₁₂ particles and the α -Mg matrix; this is more appropriately termed composite or modulus mismatch hardening. Here, we use the relationship in Eq. [9] that was developed for this mechanism by Caceres *et al.*^[16,67,71] based on the work of Brown and Clarke^[73] for disk-shaped particles of β -phase. Overall, due to the low β -phase fraction measured in these alloys and their low modulus difference, this mechanism for strengthening was determined to be very low compared to solid solution and grain boundary strengthening mechanisms even in the most concentrated alloys. The average β -phase volume

fraction through thickness is used in this calculation due to the minimal change through thickness.

$$\sigma_{disp} = 135 * f_{beta} \quad [9]$$

The predicted values found using the weighted linear superposition model defined in Eqs. [3] and [4] can be compared to the measured yield strength values. A summary of the constants used in the current linear superposition model for these Mg-Al-Mn alloys is provided in Table V, along with a comparison to the values used by other recent investigations. As shown in Figure 13, the estimated values match the experimental tensile results for both the 2.5- and 5 mm-thick plates. The goodness of fit is computed using the coefficient of determination, R^2 . The coefficient is 0.5 for the fit to both plate thicknesses, presumably due to the high intrinsic strength predicted by the $k_{y,Mg}$ coefficient, which is a constant set by the literature. This reduces the predicted slope by lowering the fit value of $k_{y,Al}$. In general, the grain boundary strengthening contributes approximately 60 to 65 pct of overall strengthening, 30 to -35 pct solid solution, and 1 to 5 pct dispersion in the 2.5 mm plates. Based on the skin thickness measurements, the skin and core are almost equal weights. For the overall grain boundary strengthening in the 2.5 mm plates, the skin is responsible for 55 pct, as compared to the core. This is similar in the 5 mm plates. The yield strength of the 5 mm plates is predicted to be lower due to the higher ESC fractions observed in the core of the plates, and increased grain size at the surface. There is a proportional decrease in both solid solution and dispersion hardening in the 5 mm plates, but a greater decrease in the grain boundary strengthening, accounting for the lower overall strength.

There is typically a range of measured values associated with yield strength for any given material. This variation can be ascribed to variations in local microstructures. This is likely related to the grain size distribution changes based on ESC occurrence and cooling rate effects in different locations. Grain boundary strengthening is the strongest strengthening mechanism in these alloys, due to the fine primary α -Mg grain size. However, significant variability is introduced due to the occurrence of ESCs in the core. A broad distribution in ESC sizes is observed, with ESCs ranging from 30 to 200 μ m in diameter. The variation in ESC size and area fraction observed within a given casting could have a significant effect on the yield strength. By varying the ESC size and area fraction, a range of strengths on the order of 5 to 10 MPa is observed. This is determined by assuming different levels of ESC fractions and average sizes. Accurate characterization of the size and fraction of ESCs generated by a given casting process is particularly important for an accurate representation of the overall grain boundary strengthening component.

Skin thickness has been shown to influence the overall yield strength.^[41] However, a precise method of determining skin thickness is still unavailable. Good correlation is observed between hardness and grain size in the

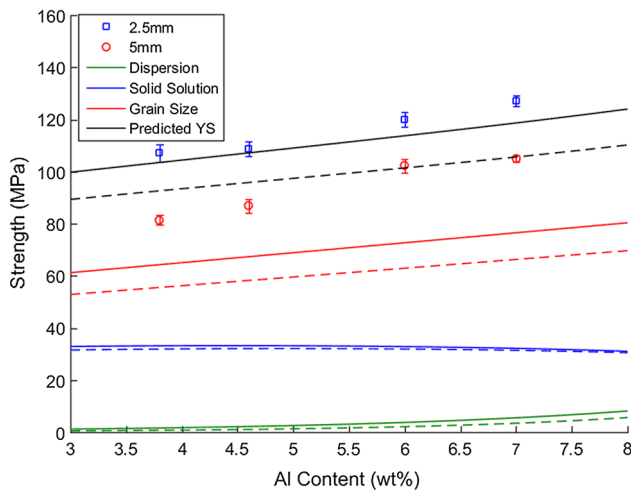


Fig. 13—The influence of alloy Al content on yield strength. The predicted yield strength from the linear superposition model is compared to the experimental data for both plate thicknesses. Predicted values for the 2.5 mm plates are shown using solid lines, and 5 mm plates using dashed lines.

2.5 mm plates, but not in the 5 mm plates. In these castings, there is a band of higher hardness at the surface; however, it is thicker than that observed by Yang *et al.* for similar compositions and thicknesses.^[40,82] A model comparing the relative hardening of the skin and core was assessed by Yang *et al.*,^[82] which predicts a skin fraction of approximately 0.10 when applied to Mg alloys with 1 to 6 wt pct Al. Sharifi *et al.* predicts a skin thickness using heat transfer rates and cooling rate–grain size relationships of 400 μm -thick in a 2.6 mm-thick casting, leading to an equivalent skin fraction of 0.3. The skin thickness is assumed to be the same for the 5 mm plates, but is complicated by the large grains frequently observed in the skin region. Significant variation in the yield strength is observed, likely due to the stochastic distribution of grain sizes observed due to the high-pressure die casting.

V. CONCLUSIONS

Quantitative characterization of microstructure and tensile behavior has been conducted for Super-Vacuum Die Cast Mg-Al-Mn alloys with a range of Al contents and two thicknesses. Based on these results, a physics-based model has been developed for predicting alloy and plate thickness effects on yield strength. This model takes into account microstructure gradients within the die casting that exist in the skin and core regions of high-pressure die castings. It also takes into account the bimodal nature of the grain structure in high-pressure die castings. The most significant effects on strength are observed to be grain boundary and solid solution strengthening. Dispersion strengthening due to the presence of $\beta\text{-Mg}_{17}\text{Al}_{12}$ particles is estimated to provide only a minimal increase in the strength.

Specific findings were:

- With increasing alloy Al content, there is an increase in the β phase fraction. This increase is lower than that predicted by a Scheil solidification model.
- In-mold grain size is independent of alloy Al content.
- Large ESCs were observed predominately in the interior regions of castings. However, in the 5 mm plates, some ESCs were observed near the casting surface.
- The tensile properties were dependent on the Al content of the alloys. With increasing Al content, the yield strength increased while both strain hardening exponent and ductility decreased.
- A physics-based yield strength model has been parameterized and predicts the experimental results reasonably well. Key features that impact the yield strength are the size and area fraction of ESCs, the solute effects on the Hall–Petch locking parameter, k_p , and solid solution strengthening.
- The yield strength was 20 to 30 MPa lower in the thicker plates. This can be quantitatively attributed to the increased area fraction of ESCs observed near the casting surface, and a slight increase in the in-mold grain size.

Note: All experimental data from this investigation are available via the Materials Commons at: <https://materialscommons.org/mcpub/#/details/238117f2-6066-4a78-a6f0-e2afdf664625>

ACKNOWLEDGMENTS

The authors are grateful to Xin Sun, Mei Li, and Joy Forsmark for many helpful discussions. Thanks to Larry Godlewski and Jacob Zindel at Ford Motor Company for providing the SVDC cast plates. The authors gratefully acknowledge funding for this project from the Department of Energy Office of Vehicle Technologies under the Automotive Lightweighting Materials Program managed by Dr. Will Joost, via subcontract with Pacific Northwest National Laboratory. The use of the Materials Commons to archive the data presented in this paper is appreciated. Funding for Materials Commons is from the U.S. Department of Energy, Office of Basic Energy Sciences, Division of Materials Sciences and Engineering under Award #DE-SC0008637 as part of the Center for Predictive Integrated Structural Materials Science (PRISMS Center) at University of Michigan.

REFERENCES

1. B.L. Mordike and T. Ebert: *Mater. Sci. Eng. A*, 2001, vol. 302, pp. 37–45.
2. A.L. Bowles, Q. Han, and J.A. Horton: *Essent. Readings Magnes. Technol.*, 2014, pp. 197–202.
3. A.A. Luo: *J. Magnes. Alloy.*, 2013, vol. 1, pp. 2–22.
4. M.M. Avedesian and H. Baker, eds.: *ASM Specialty Handbook—Magnesium and Magnesium Alloys*, ASM International, Metals Park, OH, 1999.

5. K.V. Yang, M.A. Easton, and C.H. Cáceres: *Adv. Eng. Mater.*, 2013, vol. 15, pp. 302–307.
6. M.R. Barone and D.A. Caulk: *Int. J. Eng. Sci.*, 2000, vol. 38, pp. 1279–1302.
7. J.H. Forsmark, J.W. Zindel, L. Godlewski, and A. Caliskan: *SAE Int.*, 2012, pp. 2–10.
8. C. Dørum, O.S. Hopperstad, M. Langseth, O.-G. Lademo, and S. Sannes: *SAE Tech. Pap. Ser.*, 2005, vol. 2005-01-07, p. 8.
9. J.P. Weiler, J.T. Wood, R.J. Klassen, E. Maire, R. Berkmortel, and G. Wang: *Mater. Sci. Eng. A*, 2005, vol. 395, pp. 315–22.
10. C.D. Lee: *Mater. Sci. Eng. A*, 2007, vols. 454–455, pp. 575–80.
11. K.S. Choi, D. Li, X. Sun, M. Li, and J.E. Allison: *SAE Int.*, 2013, pp. 3–10.
12. J.E. Allison, D. Backman, and L. Christodoulou: *J. Mater.*, 2006, vol. 58, pp. 25–27.
13. S. Sannes, H. Gjestland, and H. Westengen: *SAE Tech. Pap. Ser.*, 2005, vol. 2005-01-03, p. 7.
14. J.H. Forsmark, J.W. Zindel, L. Godlewski, J. Zheng, J.E. Allison, and M. Li: *Integr. Mater. Manuf. Innov.*, 2015, vol. 4, pp. 1–38.
15. U. Weiss and A. Bach: *La Metall. Ital.*, 2011, vols. 11–12, pp. 31–39.
16. K.V. Yang, C.H. Cáceres, and M.A. Easton: *Metall. Mater. Trans. A*, 2014, vol. 45A, pp. 4117–28.
17. P. Sharifi, Y. Fan, K. Sadayappan, G. Birsan, and J.T. Wood: *Magnes. Technol.*, 2015, vol. 2015, pp. 351–56.
18. I. Toda-Caraballo, E.I. Galindo-Nava, and P.E.J. Rivera-Díaz-del-Castillo: *Acta Mater.*, 2014, vol. 75, pp. 287–96.
19. C.H. Cáceres, W.J. Poole, A.L. Bowles, and C.J. Davidson: *Mater. Sci. Eng. A*, 2005, vol. 402, pp. 269–77.
20. D. Rodrigo, M. T. Murray, and H. Mao: *SAE Int. Congr. Magnes. Sess.*, 1999.
21. T.K. Aune, H. Westengen, and T. Ruden: *SAE Tech.*, 1993, pp. 51–57.
22. C.H. Cáceres and B.I. Selling: *Mater. Sci. Eng. A*, 1996, vol. 220, pp. 109–16.
23. T.D. Berman, T.M. Pollock, and J.W. Jones: *Metall. Mater. Trans. A*, 2015, vol. 46A, pp. 2986–98.
24. E.I. Barker, K.S. Choi, X. Sun, E. Deda, J. Allison, M. Li, J. Forsmark, J. Zindel, and L. Godlewski: *Comput. Mater. Sci.*, 2014, vol. 92, pp. 353–61.
25. K.S. Choi, E.I. Barker, G. Cheng, X. Sun, J. Forsmark, and M. Li: *SAE Int. J. Mater. Manuf.*, 2016, vol. 9, pp. 2016-01-0290.
26. K. Vanna Yang, M.A. Easton, and C.H. Cáceres: *Mater. Sci. Eng. A*, 2013, vol. 580, pp. 191–95.
27. T.D. Berman: University of Michigan, Ann Arbor, MI, unpublished research, 2016.
28. Materials Commons, <https://materialscommons.org/mcpub/#/details/238117f2-6066-4a78-a6f0-e2afdf664625>. Accessed 20 Aug 2016.
29. B. Puchala, G. Tarcea, E.A. Marquis, M. Hedstrom, H.V. Jagadish, and J.E. Allison: *Jom*, 2016, vol. 68, pp. 2035–44.
30. L.-Y. Wei and R. Warren: *Mater. Sci. Technol.*, 2007, vol. 23, pp. 745–52.
31. V.Y. Gertsman, J. Li, S. Xu, J.P. Thomson, and M. Sahoo: *Metall. Mater. Trans. A*, 2005, vol. 36A, pp. 1989–97.
32. J.H. Forsmark, Z. Dowling, K. Gibson, C. Mueller, L. Godlewski, J.W. Zindel, and J.M. Boileau: *SAE Int. J. Mater. Manuf.*, 2015, vol. 8.
33. C.M. Gourlay, H.I. Laukli, and A.K. Dahle: *Metall. Mater. Trans. A*, 2007, vol. 38A, pp. 1833–44.
34. N. Tahreen, D.L. Chen, M. Nouri, and D.Y. Li: *J. Alloys Compd.*, 2015, vol. 623, pp. 15–23.
35. A.L. Bowles, K. Nogita, M.S. Dargusch, and C.J. Davidson: *Mater. Trans.*, 2004, vol. 45, pp. 3114–19.
36. A.V. Nagasekhar, M.A. Easton, and C.H. Cáceres: *Adv. Eng. Mater.*, 2009, vol. 11, pp. 912–19.
37. H.I. Laukli: Norwegian University of Science and Technology, 2004.
38. H.I. Laukli, C.M. Gourlay, and A.K. Dahle: *Metall. Mater. Trans. A Phys. Metall. Mater. Sci.*, 2005, vol. 36, pp. 805–18.
39. A.L. Bowles, J.R. Griffiths, and C.J. Davidson: *Magnes. Technol.*, 2001, vol. 2001, pp. 161–68.
40. K. Vanna Yang, C.H. Cáceres, and M.A. Easton: *Mater. Sci. Eng. A*, 2013, vol. 580, pp. 355–61.
41. J.P. Weiler, J.T. Wood, R.J. Klassen, R. Berkmortel, and G. Wang: *Mater. Sci. Eng. A*, 2006, vol. 419, pp. 297–305.
42. H. Cao and M. Wessén: *Metall. Mater. Trans. A*, 2004, vol. 35A, pp. 309–19.
43. M.S. Dargusch, M. Nave, S.D. McDonald, and D.H. StJohn: *J. Alloys Compd.*, 2010, vol. 492, pp. L64–68.
44. S. Barbagallo, H.I. Laukli, O. Lohne, and E. Cerri: *J. Alloys Compd.*, 2004, vol. 378, pp. 226–32.
45. W.P. Sequeira, G.L. Dunlop, and M.T. Murray: in *Proc. Third Int. Magnes. Conf.*, 1996, pp. 63–73.
46. D.J. Sakkinen: *SAE Tech. Pap.*, 1994, pp. 558–69.
47. D. Mirković and R. Schmid-Fetzer: *Metall. Mater. Trans. A Phys. Metall. Mater. Sci.*, 2009, vol. 40, pp. 974–81.
48. X.J. Wang, S.M. Zhu, M.A. Easton, M.A. Gibson, and G. Savage: *Int. J. Cast Met. Res.*, 2014, vol. 27, pp. 161–66.
49. K. Sadayappan, W. Kasprzak, Z. Brown, L. Ouimet, and A.A. Luo: *Mater. Sci. Forum*, 2009, vols. 618–619, pp. 381–86.
50. M. Zhou, A. Yu, N. Li, H. Hu, and R. Bowers: *Magnes. Technol.*, 2006, vol. 2006, pp. 121–27.
51. X. Li, S.M. Xiong, and Z. Guo: *Mater. Sci. Eng. A*, 2015, vol. 633, pp. 35–41.
52. S. Otarawanna, C.M. Gourlay, H.I. Laukli, and A.K. Dahle: *Mater. Charact.*, 2009, vol. 60, pp. 1432–41.
53. S.G. Lee, G.R. Patel, and A.M. Gokhale: *Scr. Mater.*, 2005, vol. 52, pp. 1063–68.
54. M.S. Dargusch, K. Pettersen, K. Nogita, M.D. Nave, and G.L. Dunlop: *Mater. Trans.*, 2006, vol. 47, pp. 977–82.
55. P. Bakke, K. Pettersen, and H. Westengen: *Magnes. Technol.*, 2003, vol. 2003, pp. 171–76.
56. N. Tahreen, D.L. Chen, M. Nouri, and D.Y. Li: *Mater. Sci. Eng. A*, 2014, vol. 594, pp. 235–45.
57. G. Cheng, E.I. Barker, E.V. Stephens, K.S. Choi, and X. Sun: *MRS Adv.*, 2016, pp. 1–12.
58. E. Aghion, N. Moscovitch, and A. Arnon: *Mater. Sci. Eng. A*, 2007, vol. 447, pp. 341–46.
59. W.P. Sequeira, G.L. Dunlop, and M.T. Murray: in *Proc. 3rd Magnes. Conf.* 1996, pp. 63–73.
60. D.G. Leo Prakash and J. Regener: *J. Alloys Compd.*, 2008, vol. 464, pp. 133–37.
61. T.N. Baker: in *Yield, Flow Fract. Polycrystals*, 1982, pp. 235–73.
62. A.J. Ardell: *Metall. Trans. A*, 1985, vol. 16A, pp. 2131–65.
63. S.C. Weakley-Bollin, W. Donlon, W. Donlon, C. Wolverson, J.E. Allison, and J.W. Jones: *Metall. Mater. Trans. A*, 2004, vol. 35A, pp. 2407–18.
64. C.H. Cáceres, C.J. Davidson, J.R. Griffiths, and C.L. Newton: *Mater. Sci. Eng. A*, 2002, vol. 325, pp. 344–55.
65. T.N. Baker, ed.: *Yield, Flow, and Fracture of Polycrystals*, 1983.
66. P. Sharifi, Y. Fan, H.B. Anaraki, A. Banerjee, K. Sadayappan, and J.T. Wood: *Metall. Mater. Trans. A*, 2016, vol. 47, pp. 5159–5168.
67. J.A. Yasi, L.G. Hector, and D.R. Trinkle: *Acta Mater.*, 2010, vol. 58, pp. 5704–13.
68. R.L. Fleischer: in *Strength. Met.*, D. Peckner, ed., 1964, pp. 93–140.
69. C.H. Cáceres and P. Lukac: *Philos. Mag.*, 2008, vol. 88, pp. 977–89.
70. J.H. Shen, Y.L. Li, and Q. Wei: *Mater. Sci. Eng. A*, 2013, vol. 582, pp. 270–75.
71. C.H. Cáceres and D.M. Rovera: *J. Light Met.*, 2001, vol. 1, pp. 151–56.
72. E.O. Hall: *Proc. Phys. Soc. A*, 1951, vol. 64, pp. 747–53.
73. N.J. Petch: *J. Iron Steel Inst.*, 1953, vol. 174, pp. 25–28.
74. A. Akhtar and E. Teghtsoonian: *Acta Metall.*, 1969, vol. 17, pp. 1339–49.
75. W.B. Hutchinson and M.R. Barnett: *Scripta Mater.*, 2010, vol. 63, pp. 737–40.
76. K. Fukuda, Y. Koyanagi, M. Tsushida, H. Kitahara, T. Mayama, and S. Ando: in *9th Pacific Rim Int. Conf. Adv. Mater. Process.*, 2016, pp. 794–96.
77. J. Zhang and S.P. Joshi: *J. Mech. Phys. Solids*, 2012, vol. 60, pp. 945–72.
78. F.E. Hauser, P.R. Landon, and J.E. Dorn: *Trans. Am. Inst. Mining, Metall. Pet. Eng. Inc.*, 1956, vol. 206, pp. 589–93.
79. C.H. Cáceres, G.E. Mann, and J.R. Griffiths: *Metall. Mater. Trans. A*, 2011, vol. 42A, pp. 1950–59.

80. P. Sharifi, Y. Fan, J.P. Weiler, and J.T. Wood: *J. Alloys Compd.*, 2014, vol. 605, pp. 237–43.
81. K.J. Kurzydłowski and J.J. Bucki: *Acta Metall. Mater.*, 1993, vol. 41, pp. 3141–46.
82. K. Vanna Yang, C.H. Cáceres, A.V. Nagasekhar, and M.A. Easton: *Mater. Sci. Eng. A*, 2012, vol. 542, pp. 49–55.
83. A. Akhtar and E. Teghtsoonian: *Acta Metall.*, 1969, vol. 17, pp. 1351–56.